UNIVERSITÀ DEGLI STUDI DI PADOVA

Dipartimento di Fisica e Astronomia "Galileo Galilei"

Corso di Laurea in Fisica

Tesi di Laurea

10 years of Surface radiation balance/Albedo properties collected in an Arctic Region

Relatore

Prof. Cinzia Sada

Correlatore

Dr. Angelo Lupi

Laureando

Anna Baldo

Anno Accademico 2020/2021

Abstract

This thesis presents the results of observations of selected fluxes of the surface radiation balance (in terms of shortwave and longwave fluxes) in north-western Spitsbergen in the years from 2010 to 2021. Measurements were taken in Ny-Ålesund, at the CCTower infrastructure, taking account the different surface types occurring in the Polar zone (snow and tundra), capturing substantial differences in the radiation balance among the various types of surface. Special attention is dedicated to melting season, and if and how it has changed during the last years, also comparing the results with similar and longer data-sets (i.e. BSRN at the AWI station). Diurnal, annual and multi-annual variations are investigated, in order to characterize the Arctic Albedo properties.

Contents

Introduction

Arctic and Antarctic combined together represent a wide portion of the Earth's cryosphere, encompassing 69% of the world's glacier area, meaning ice sheets, sea ice and land area with the most persistent snow cover. Even though the polar regions are located at the furthermost edges of our world, they highly interact with the rest of the planet, through the ocean and the atmosphere, sharing ecological and social systems, and are proving to be among the areas most influenced by the changes in our climate.

As described in the latest IPCC report, it is very likely that the Arctic has warmed at more than twice the global rate over the past 50 years, and it is virtually certain that surface warming in the Arctic will continue to be more pronounced than the global average warming over the XXI century [2]. Given the strong interconnection with the rest of the planet, the wide dimensions of the area considered and the multiple feedback mechanisms that can be triggered between the different components of the environment, it is a challenge to define which agents led to the phenomenon known as Arctic amplification and the exact impact of each of them. Among the investigated topics there are: reduced summer albedo due to sea ice and snow cover loss, the increase of total water vapour content in the Arctic atmosphere, changes in total cloudiness in summer, additional heat generated by newly formed sea ice across wider open water areas in the autumn, northward transport of heat and moisture and the lower rate of heat loss to space from the Arctic relative to the subtropics ([3], [4], [5], [6]). All of these processes are to be investigated, since their impact is not only relegated to the Arctic through local feedbacks with the ice and land surface, but also tightly connected with the global energy balance of the planet. Since radiative fluxes represent the main driver of such processes, it is essential to have reliable measurements in order to study and comprehend surface radiation budget and its changes. Climate Change Tower (CCT) in Ny-Ålesund is an example of scientific station that collects such measurements.

Aim of this thesis is to use the data collected at CCT and analyse part of the radiative fluxes and their evolution in the years from 2010 to 2021. Starting from the single measurements, it will be necessary to build averages of such values in order to move from daily to monthly to seasonal to yearly trends, finally leading to a climatological time scale. Moreover, the melting season will be specifically investigated: being the time of the year when the snow on the ground melts and reveals the underlying tundra, changes in its duration and timing can in fact bring significant modification in vegetation growth and related animal behaviour. In this thesis the method chosen to examine such topics is the study of surface albedo. The results will be then compared with the ones obtained on different data-sets by similar studies, such as the ones led by the German "Alfred Wegener Institute" (AWI) and the Italian "Istituto di Scienze Polari" (ISP).

1 Radiation fundamentals

Electromagnetic radiation in vacuum may be viewed as an ensemble of waves propagating at the speed of light, that is $c = 2.998\,10^8$ m/s. Any wave can be characterized by its wavelength, λ, and frequency, ν. Since radiative transfer in planetary atmospheres involves waves with a continuum of wavelengths and frequencies, the energy carried by the radiation can be partitioned in the contributions from various areas of the spectrum, identified with wavelengths bands. Hence the radiation can be defined as *shortwave* when $\lambda < 4\mu m$, while it is called *longwave* if $\lambda > 4\mu m$.

Since radiation can theoretically be transmitted, absorbed and reflected by a single body, in order to derive some explanatory laws it is sometimes easier to make some simplifying hypothesis. Historically, radiation has been studied through the concept of *blackbody*, i.e. a surface that completely absorbs incident radiation. Some typical examples are dark materials such as coal or large cavities with a small aperture, through which little radiation manages to enter and subsequently escape, reflecting many times within the cavity until completely absorbed. It has been determined that the intensity of radiation emitted by a blackbody is rightfully represented by the Planck's law. A corollary of such law, also known as Wien's displacement law, states that there is a relationship between temperature of a body T and the wavelength of the maximum spectral radiance λ_{max}, so that

$$\lambda_{max} = \frac{2897\mu mK}{T} \tag{1}$$

It is therefore possible to associate the two different ranges of radiation to two principal sources. In fact, for a body of about $5800\,K$, such as the Sun, the spectral radiance is confined between $0.4 - 4\,\mu$m, which means the radiation belongs to the visible and near infrared regions of the spectrum. For a significantly cooler body such as the Earth, whose medium temperature can be approximated as $250\,K$, radiation is largely confined in the infrared, with Wien's law locating the peak at about $12\,\mu m$. Therefore we associate the shortwave radiation to the Sun and the longwave to the Earth, as it will be discussed in the following chapter.

In order to characterize the amount of energy emitted by a source or received by an object, it is necessary to introduce two physical quantities and a frame of reference where to identify the relative position of source and object in space.

The position of any point on the surface of the Earth can be identified by two angles and using the observer's local horizon as the fundamental plane. The first is *zenith* θ, which is the angle between Zenith, i.e. the point on the celestial sphere located on the observer's ascending vertical, and the direction in exam. The second is *azimuth* ϕ, that is the angle between the North on the local meridian and the position of the point on the Earth's surface. Since, in the case studied in this thesis, the Sun acts as the source and the Earth as object, the zenith angle is referred to the Sun's position in Earth's sky and therefore called "solar zenith angle" or "SZA", while the azimuth is referred to as "AZI".

Radiance, identified as I, is defined as the power emitted by a source per unit of the solid angle and per unit of the projected surface of an extended widespread source in a given direction. Given the radiant energy dE_λ, associated to an interval of wavelengths $[\lambda,\, \lambda + d\lambda]$, it crosses in unit time an element of area dA, associated to a solid angle $d\Omega$ and whose orientation in space is identified by the angle θ between the normal to the projected surface an the direction of the source (i.e. the zenith

angle). The monochromatic radiance at λ is therefore defined as

$$I_\lambda = \frac{dE_\lambda}{d\Omega dA cos\theta} \tag{2}$$

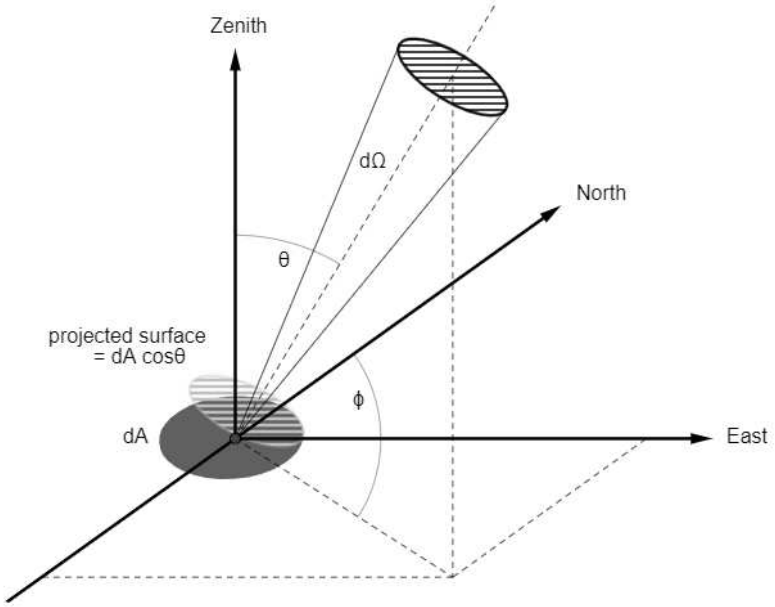

Figure 1: Frame of reference with zenith θ and azimuth ϕ angle and projection of the surface dA identified by a widespread object in a given direction from the plane

Irradiance (or flux density), identified as F, instead, is defined as a measure of the rate of power received per unit area by radiation with a given wavelength through a plane surface from the entire half-space above it. Therefore, given the radiant energy dE_λ that crosses an element of area dA per unit time,

$$F_\lambda = \frac{dE_\lambda}{dA} = \int_{2\pi} I_\lambda cos\theta d\Omega = \int_0^{2\pi} \int_0^{\frac{\pi}{2}} I_\lambda(\theta, \phi) cos\theta sin\theta d\theta d\phi \tag{3}$$

where $d\Omega$ represents an elemental arc of solid angle, θ is the angle between the incident radiation and the direction normal to dA, also identified with the zenith angle, and ϕ, in the frame of reference defined above, is the azimuth angle. The integration is over 2π steradians because, opposite to radiance, irradiance is not directional: while the energy coming from the Sun actually arrives from a specific direction, it is scattered because of the atmosphere all over the width of the visible sky, therefore the ground (and the sensor) receives radiation from the half-space above it, that is an entire hemisphere with solid angle 2π. The factor $cos\theta$ represents the spreading and resulting dilution of radiation with a slanted orientation relative to the surface. The total radiance and irradiance are obtained by integrating the monochromatic quantities over the electromagnetic spectrum.
Combining such definitions with the above mentioned characterisation of radiation on the basis of wavelength, both shortwave (SW) and longwave (LW) radiation have an upward and downward component. Shortwave irradiance is in fact incoming from the Sun and reflected by the Earth and can be written as $SW^\downarrow$ and $SW^\uparrow$ respectively. Longwave upward radiation $LW^\uparrow$, instead, is the one emitted by the Earth and the downward component $LW^\downarrow$ is the one absorbed and re-emitted by the clouds. The total amount of radiation that the Earth gains and loses is called the net radiation budget and is

defined as

$$Q_{net} = (SW^{\downarrow} - SW^{\uparrow}) + (LW^{\downarrow} - LW^{\uparrow}) \tag{4}$$

It is possible to talk about reflected radiation because the Earth is clearly not an example of blackbody, therefore, as it receives radiant energy from the Sun, a portion of such energy is reflected and diffused from the surface of the planet back towards space. The physical quantity that describes such ratio is albedo. In case of broadband albedo, computed considering all the wavelengths of the spectrum, it is given by

$$\alpha = \frac{F^{\uparrow}}{F^{\downarrow}} \tag{5}$$

where $F^{\uparrow}$ is the reflected irradiance and $F^{\downarrow}$ the incident one. Since the incoming radiation that gets reflected is the solar one, hence in the shortwave range, albedo is often described as $\frac{SW^{\uparrow}}{SW^{\downarrow}}$. Albedo varies between 0 and 1, where the first value corresponds to a a black body that absorbs all incident radiation and the second to a body that reflects it all.
Such reflection is influenced either by the nature of the surface or by the angular distribution of the incoming radiation. For example, the snow cover on the ground is a factor that strongly affects albedo: when the ground is covered by snow and becomes white, its capability of reflecting the light is enhanced and therefore the albedo rises. On the contrary, considering a mostly dark surface, for example a dark wet soil covered in vegetation or the ocean, albedo drops since most of the incident radiation gets absorbed instead of reflected. Moreover, reflection over snow and ice (or in general over materials easily eroded and shaped by persistent winds) also depends on the position of the Sun in the sky. A phenomenon typical of high latitudes is in fact the presence of "sastrugi", ice ridges culminating in a point shaped extremity aligned along the direction of the main wind. Such formations imply the presence of more shaded areas compared to others while the Sun crosses the sky during Earth's daily rotation. This factor affects the quantity of light actually reaching certain areas of the ground and consequently how much of it gets reflected.

Guided by such observations and by the characteristics of the site in exam, in this thesis the albedo will play a key role in identifying some crucial moments in the Arctic year. In fact, looking at how the albedo varies through the months, it is possible to determine when the snow covering the Svalbard grounds melts to reveal the underlying tundra and how this melting window varies and shifts through the years.

2 Measurement site and instruments

2.1 Measurement site

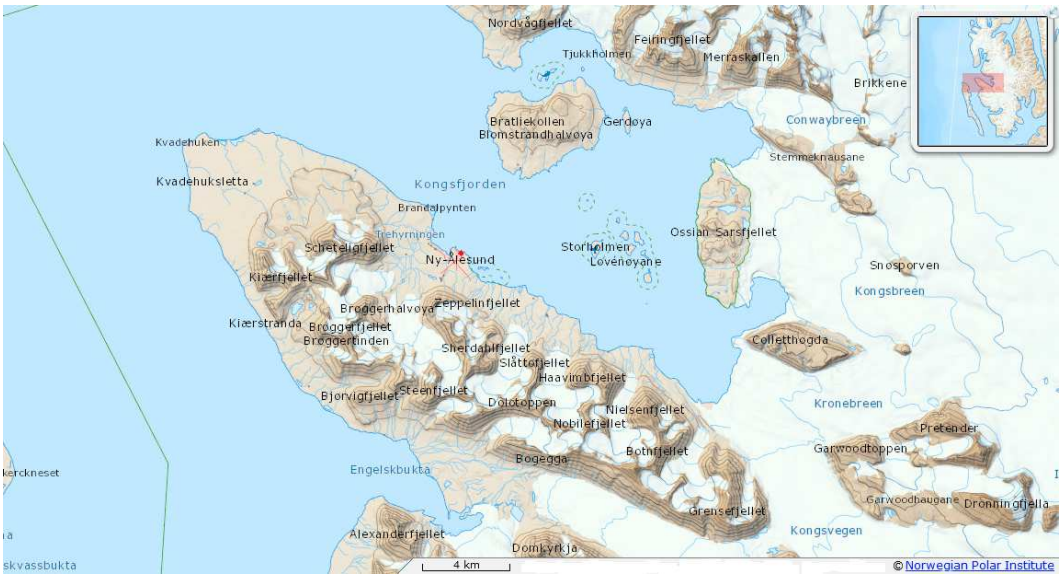

Figure 2: Kongsfjorden, the Brøgger peninsula and Ny Ålesund (red dot) [14]

The data analyzed in this thesis have been collected from 2010 to 2020 by instruments installed on the Climate Change Tower, a scientific platform managed by the National Research Council of Italy and located 2 km apart from a Norwegian village called Ny-Ålesund on Spitsbergen, in the Svalbard archipelago. Ny-Ålesund's coordinates are 78.9235° North and 11.9099° East, which means the village is widely above the Arctic Circle and therefore it experiences during the course of the year months of never-ending daylight called "polar day", approximately between mid-April and the end of August, and months of constant night called "polar night" between the end of October and mid-February. The town is located on a peninsula on the southern shore of Kongsfjorden (literally "the King's Bay"), a fjord oriented NW-SE on the west coast of Spitsbergen. In the middle of the peninsula there is a ridge of medium-low elevation (the highest peaks are at the topmost SE of the chain, reaching slightly above 1000m), framing the village along the western to south-eastern direction.

The CCT is equipped with a set of meteorological sensors installed at different heights to provide continuous measurements of atmospheric parameters such as temperature, relative humidity, pressure, wind speed and radiation.
The structure is composed of 17 modules, equipped with patch boxes to provide a power supply and data connection that ends in a dedicated hut at 40 m from the tower, where the acquisition systems are located. The CCT provides continuous profiles of meteorological parameters at four levels up to 34 m, while measurements of turbulent fluxes, moisture

Figure 3: Climate Change Tower, Ny Ålesund [13]

and of radiation balance components (visible and infrared) are taken at two levels. Measurements of the characteristics of the snow layer (depth and temperature) are also provided along with the atmospheric parameters [13].

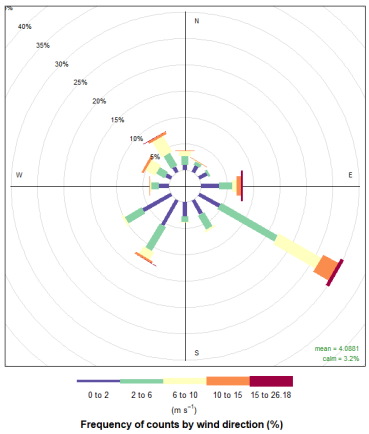

Figure 4: Wind-rose realized using wind speeds and directions collected at 32m in 2019

As expected, the mountainous area strongly influences the direction and speed of the wind that reaches the village, measured along the tower at 32 m, 10 m, 4 m and 2 m above ground level. Winds are characterized by a strong NW-SE component during all the months of the year. Wind flows most frequently and with the highest speed from E-SE, especially in the winter months, moving seawards from the Kronebreen and Kongsvegen glaciers. During the whole year and gaining strength in the summer months, wind also blows from S-SW, flowing down from the Broggerbreen glaciers that lie on top of the ridge. The last wind sector that emerges from measurements is from N-NW, coming from the open sea, even though it is a weaker wind compared to the others. Its wind speeds rarely reach over 6 m/s, while SE winds often reach speeds higher than 10 m/s, even touching nearly 30 m/s during the colder months.

Temperature, similarly to the wind, is measured at the same four heights along the tower. It oscillates with the seasonal cycle during the year in a range spanning on average from $-10°$ C in the winter months to 10° C in summer. Ny Ålesund's climate is in fact mitigated by the presence of the ocean and from the last remnant of the Gulf Stream, but more extreme temperatures have been registered, with record highs reaching nearly 20° C in summer 2020 and record lows reaching $-31°$ C in winter 2020.

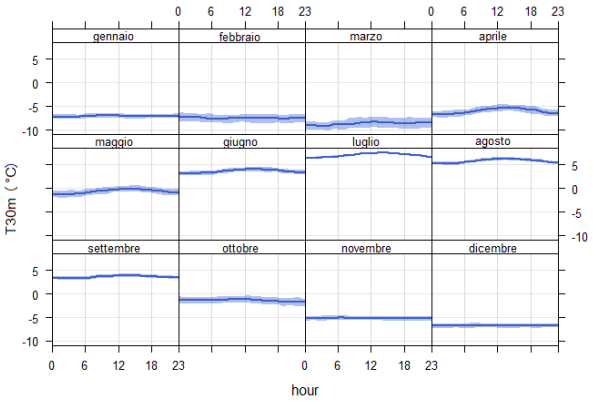

Figure 5: Hourly temperature at 32 m averaged in 2010–2020, shaded area is 95% confidence interval in the mean

2.2 Instruments

Radiation instruments are installed at two levels. At the top of the tower (33.4 m a.g.l.) on an outstretched arm pointing south there is a Kipp and Zonen net radiometer model CNR1, installed in October 2009 and characterised by a 10% accuracy. Upward radiation fluxes, emitted and reflected by the surface, are also measured some meters below (25 m a.g.l.) on a southerly oriented arm with two downward-looking Kipp and Zonen first class radiometers, a CM11 pyranometer for SW and a CG4 pyrgeometer for LW, both featuring a 3% accuracy on the data collected per minute and on the daily total. This is due to the fact that, over a wider time window to integrate on, some variations cancel

each other out. This configuration is assumed to compensate for the low accuracy of the CNR1 with respect to the accuracy of higher class radiometers. Measurements are collected once a minute and recorded along with the date and time they have been taken.

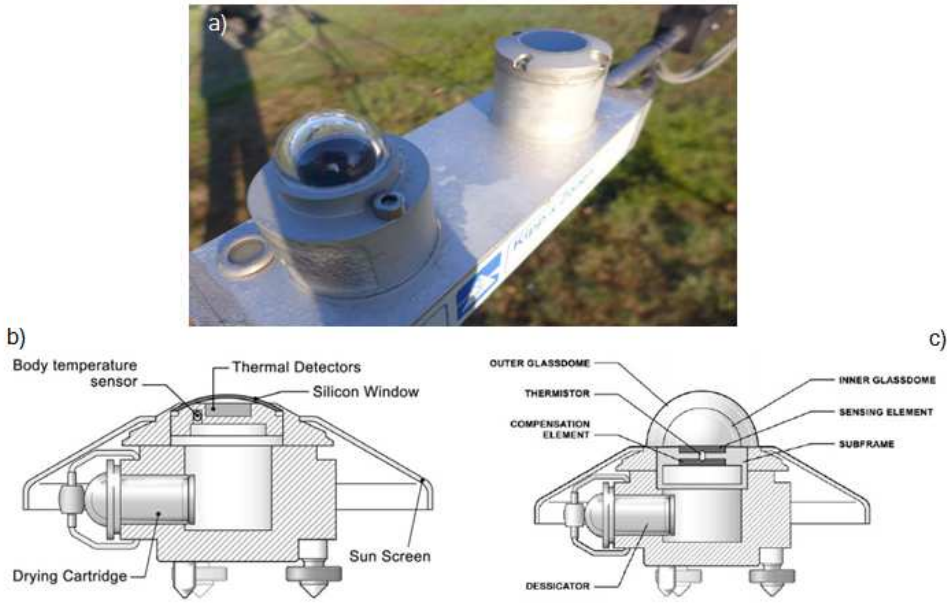

Figure 6: a) Kipp and Zonen net radiometer model CNR1 [20], b) Kipp and Zonen CG4 pyrgeometer [19] and c) Kipp and Zonen CM11 pyranometer schematic construction [18]

	CM11	**CNR1:CM3**
Spectral range	340-2200 nm	305-2800 nm
Sensitivity	4-6μV/Wm^{-2}	10-35μV/Wm^{-2}
Temperature dependence of sensitivity	<1% (-10°C to +40°C)	±6% (-10°C to +40°C)
Zero offset type A	12 W/m^{2*}	+15W/m^{2*}
Accuracy (for daily totals)	3%	10%
Field of view	180°	180°
Operating temperature	-40°C to +80°C	-40°C to +80°C
	CG4	**CNR1:CG3**
Spectral range	4.2 to 45 μm	4.5 to 42 μm
Sensitivity	10μV/Wm^{-2}	5-18μV/Wm^{-2}
Temperature dependence of sensitivity	Max ±1% (-20°C to +50°C)	±6% (-10°C to +40°C)
Window heating offset	Max 4W/m^{2**}	Max 25W/m^{2**}
Accuracy (for daily totals)	3%	10%
Field of view	180°	150°
Operating temperature	-40°C to +80°C	-40°C to +80°C

Table 1: Technincal data of CM11, CNR1-CM3 (pyranometer), CG4 and CNR1-CG3 (pyrgeometer)

Meteorological sensors with 1 minute acquisition rate are placed at four levels and each set includes a Vaisala thermo-hygrometer model HMP45AC and a Young Marine wind sensor model Wind Monitor 05106. The two instruments are mounted facing north on the same arm, about 0.5 and 1.5 m off the tower. The accuracy of the temperature measurements varies between ±0.4°C at −20°C and ±0.2°C at 20°C. The accuracies of wind speed and direction are ±0.3 m/s or 1% of reading and ±3° respectively.

*to 200W/m^2 thermal radiation
**to 1000 W/m^2 normal incidence solar radiation

3 Data analysis

3.1 Data organisation and cleaning

The measurements analyzed in this thesis have already been collected in Ny Ålesund over the course of the years and are stored in a CNR server in Bologna [17]. They have been analyzed using the software R.

Not all the data collected by the instruments at CCT are necessary for this study, therefore the first step is to select only the columns of interest and create a final dataframe to work on. Once the radiation data are identified, it is possible to actually compute the albedo per minute, already defined as the ratio between shortwave radiation directed upwards and downwards. Since the CNR1 measures radiation going in both directions while CM11 only measures upwards radiation, the two resulting albedo values are computed as

$$\alpha_{CNR1} = \frac{SW^{\uparrow}_{CNR1}}{SW^{\downarrow}_{CNR1}} \qquad \alpha_{CM11} = \frac{SW^{\uparrow}_{CM11}}{SW^{\downarrow}_{CNR1}} \tag{6}$$

Radiometers also measure longwave radiation, but such measurements must subsequently be corrected with the irradiance of the instrument itself, a consequence of the fact that the instrument has its own temperature and therefore emits radiation. The Stefan-Boltzmann law states that the irradiance is related to the body temperature according to $F = \sigma T^4$, with $\sigma = 5.6710^{-8}\, Wm^{-2}K^{-4}$ being the Stefan-Boltzmann constant. The corrected longwave data is obtained adding to the measured irradiance the one of the radiometers according to such law, given the temperature of the instruments.

The resulting values are therefore cleaned: it is first necessary to eliminate computational errors or values that, given a too small $SW^{\downarrow}$ due to an anomalous instrumental reading, resulted in an infinite albedo. Once rejected the infinities, a specifically designed function associates the position of the Sun in the sky to each collected date and time of the day [7]. Such function, knowing the coordinates of Ny Ålesund, returns a vector containing the SZA and the AZI of the Sun in each moment the data were collected. Once such vector has been added to the dataframe, another filter is applied to the albedo values: all values associated to a SZA higher than 83° are rejected. Such decision is due to the fact that the most significant contribution to radiation comes from direct radiation from the Sun, which directly depends on the cosine of the average solar zenith angle. When the Sun is low on the horizon, the SZA is at its highest, its cosine is at its minimum therefore small quantity of radiation reaches the sensor, since the projected surface upon which radiation gets diluted is the widest. Data collected in these scenarios are bound to be unreliable. Then, in order to eliminate also unreliable values deriving from scarcely lit days, which include both thickly clouded days at the edges of polar night and days when the sun was too low on the horizon, therefore covered by the mountains, all the values associated to SWD < 50 W/m^2 are rejected. Finally, in order to operate only with values with physical meaning, all albedo values lesser than 0 or higher than 1 are rejected as well. All the values rejected during this procedure are set to "NA".
If there is a time window where data has not been collected because the instrument was not working or was not operative in the first place, it is already registered as "NA".

3.2 Instrumental analysis

At this point, in order to check on their proper functioning and ensuring the reliability of the data collected, a few tests and analysis have been run on all the measurements collected in 2010.

3.2.1 Shortwave radiation

Shortwave radiation has been investigated first. In order to check the consistency of the measurements of upwards SW radiation ($SW^{\uparrow} \equiv$ SWU) taken by the two sensors (CNR1 and CM11), the following scatterplot and residual analysis have been produced, where the residuals are defined as the difference between the measurements taken from the CNR1 and the expected values, i.e. those of the linear interpolation.

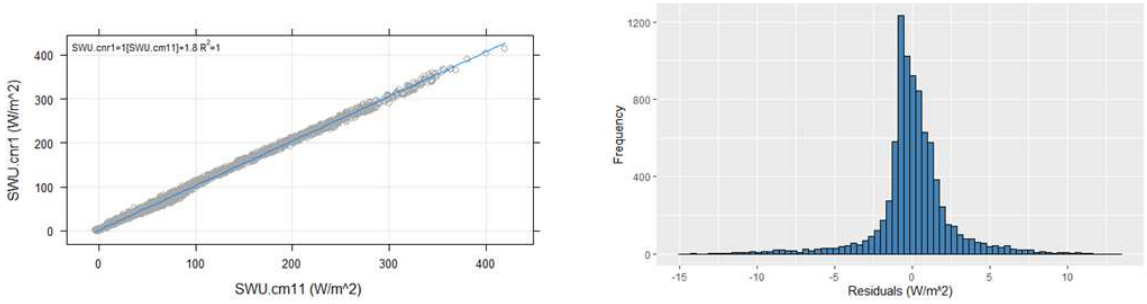

Figure 7: Scatterplot of SWU collected by CNR1 and CM11 sensors in 2010 and histogram of residuals

As visible from the scatterplot, measurements collected by the two sensors show an R^2 value equal to 1. Such coefficient is in fact the squared value of the correlation coefficient, which confirms the visible linear correlation of the two values. There is also a shift between the two, with measurements collected by the CNR1 being slightly higher than the ones collected by the CM11. Knowing the relative position of the two sensors, this could be due to the bigger area covered by the CNR1, located on top of the CCT at ~ 34 m. Data collected by the CNR1 are also affected by a bigger uncertainty compared to the data collected by the CM11, since the first instrument has an accuracy of 10% compared to the 3% of the second. Comparing the highest values of the residuals with the 10% of the highest SWU measurements taken by CNR1, residuals fall within the margin of such uncertainty. Moreover, the histogram of residuals shows how they are distributed according to a Gaussian-looking distribution, centered upon the mean value of zero. Residuals are therefore assumed to be randomly distributed, excluding the hypothesis of systematic errors in one of the two sensors. The same analysis run on 2020 data resulted in a regression line of $SWU.cnr1 = 1.1[SWU.cm11] + 1.8$ and $R^2 = 1$, thus the correct functioning of the instruments is assumed to be maintained throughout the years.

3.2.2 Albedo

The second parameter investigated is the albedo itself, first computed per minute and then averaged over a time span of one hour.
Once the aforementioned cleaning of such values has been done, there are some periods of the year where the data is not available anymore, adding to the days where data wasn't available in the first place. A quick way to visualize the amount of available data is a summary plot. In Figure 8 the albedo per minute computed using measurements from 2010 from CNR1 and CM11 is shown.

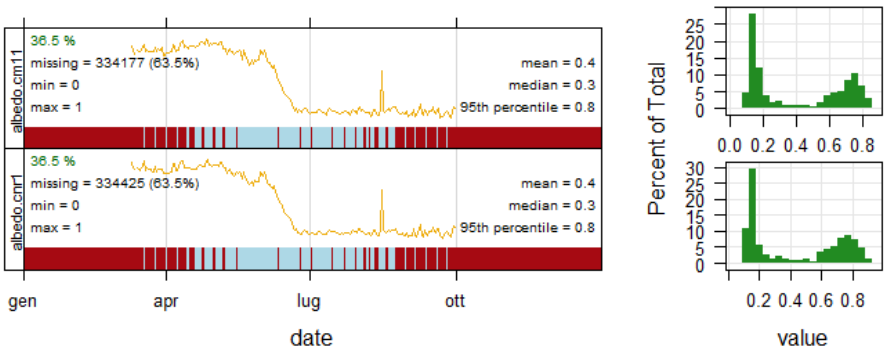

Figure 8: Summary-plot of albedo values per minute collected by the two sensors in 2010

The red and blue bar at the bottom of the graphic represents the missing (red) and available (blue) data during the course of the year, quantified by the percentages showed on the left. The yellow line represents the daily average and some statistical information are also plotted on the sides, such as maximum, minimum, mean, median, $95th$ percentile. The plots on the right are frequency histograms of the analyzed measurements. As forseen, all the data registered during the polar night period, i.e. between mid-October and mid-February, are discarded, as there is no shortwave incoming that the sensors could have possibly measured. Moreover, all the data coming from days with Sun at SZA < 83, that is until the beginning of March and from the beginning of October onwards, are discarded as well. Lastly, all the thin red lines in the spring-summer period represent the data rejected because of low incoming radiation or non-physical albedo values.

Having said that, in order to work with a lighter and more easily interpretable dataset, hourly averages have been computed and plotted over the course of the year, as shown in Figure 9.

The tendency follows the anticipated pattern and can be subdivided in three separate periods: the first ranging from mid-March to mid-May, the second from mid-May to late June and the third spanning from late June to the beginning of October.

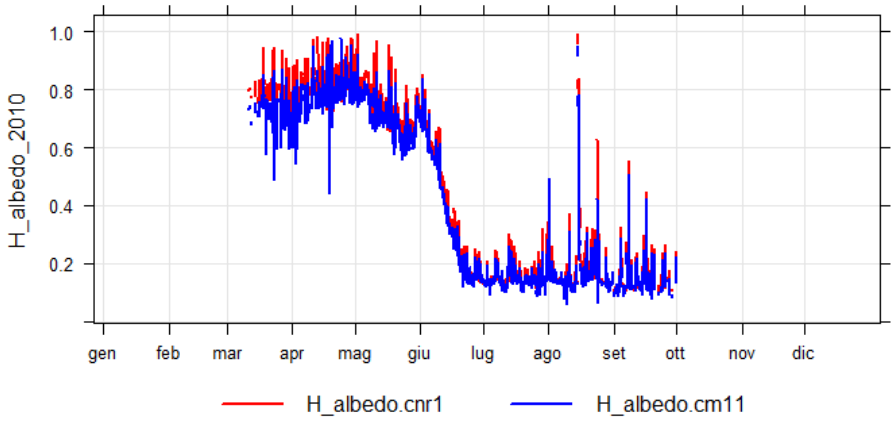

Figure 9: Hourly albedo values collected during the year 2010 from the two sensors

As previously mentioned, these sections are directly related to the nature of the ground surrounding the CCT. During the spring months, when snow covers the ground evenly and consistently, most of the incoming radiation gets reflected, resulting in a high albedo around 0.8, while during the summer months, when the snow is gone and the underlying tundra is revelaed, radiation gets absorbed rather than reflected and the albedo drops to $\sim 0.1 - 0.2$. The spikes visible during the summer represent the occasional snowfalls that took place in August and September, covering the ground for a couple

of days and bringing the albedo back around spring values, but melting or being blown away quickly, as the albedo drops back to the seasonal average. The intermediate period is the melting window, when the spring is turning into summer, snowfalls are rarer (but still take place, as the spike at the beginning of June testifies) and temperature rises, melting the snow on the ground. The snow cover goes from uniform to uneven and as the snow patches shrink and disappear the albedo transitions between spring and summer values.

There is only one unexpected pattern, located at the very beginning of the time series, which is present also in other years analyzed: the albedo during March is lower than in April, while snow cover conditions don't significantly change. This strange fact has been explored and has been attributed to the relative position of the CCT and the ridge that crosses the Brøgger Peninsula. During February and March, the first months where the Sun actually rises above the horizon, the mountain ridge that crosses the peninsula shields Ny Ålesund and the CCT, blocking out direct radiation from the sensors that only collect scattered light from the rest of the sky. That means that a non-negligible part of the albedo is missing. The albedo has in fact a more sophisticated definition, resulting as the sum of a term called "black sky" albedo, that is the albedo computed only considering the radiation coming directly from the Sun beam at a definite position in the sky, and a "white sky" albedo, the term that, on the contrary, computes the albedo from the diffused light coming from the rest of the sky, summing up to form the so called "blue sky" albedo. Since during March one of the components is missing, albedo is lower than in April, when the Sun rises above the ridge and the instruments see it directly. As predictable, CM11 values are systematically slightly lower than CNR1 values, reflecting the same tendency of the SWU measurements. That being said, the data computed using the values from the two sensors fluctuate coherently, once again confirming the correct functioning of both the instruments and the reliability of the measurements collected.

3.2.3 Solar zenith angle

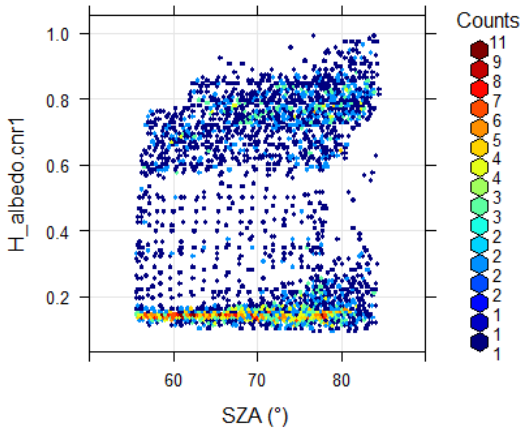

Figure 10: Hourly averaged values for albedo as a function of SZA during the year 2010

Hourly albedo and SWD dependency on SZA is explored next.

Figure 10 shows a scatterplot of hourly albedo averages on SZA values. The two main clusters represent albedo values collected before (higher) and after (lower) the melting. The lower cluster shows that, during the whole movement of the Sun in the sky (reaching a minimum of SZA $\sim 55°$) happening on polar days in summer, albedo stays nearly constant. The higher cluster instead is slightly tilted: this is due to the fact that, as observed above, the albedo during the spring reaches its highest value in April, when the Sun still sets and therefore reaches high SZA values.

Nevertheless, during the first stages of the melting, that take place in polar day conditions already (i.e. in low SZA), albedo reaches the ~ 0.7 values quite often, hence explaining the tilt. Vertical lines represent the albedo transition period instead, happening already in polar day conditions, when the

Sun covers the whole spectrum of SZA. The band-like aspect is due to the fact that hourly averages were used and the Sun therefore moves in one-hour steps in the sky.
Figure 11 shows instead how SWD (i.e. $SW^{\downarrow}$) depends from the SZA. As expected, high SZA days coincide with little SWD values, as the Sun emerging from the horizon dilutes its light on a wide area. Those values are also the ones reached more often during the year, when the sun sets, rises or brushes the horizon in summer nights. As it rises daily, reaching higher SZA values, SWD rises as well, but the whole spectrum is covered even for minimum SZA values: there are in fact days with more or less cloud overage, that acts as a more or less effective shield for the sunlight, that gets absorbed before hitting the ground. The tilted straight line that follows the upper margin of the cluster represents the clear sky conditions, where the maximum SWD is received on the ground.

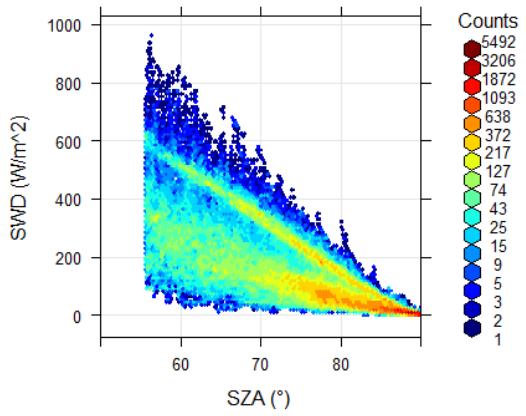

Figure 11: SWD values per minute collected in 2010 as a function of SZA

3.2.4 Azimuth angle

Next comes the relation between the albedo, SWD and the AZI values. In this case, albedo per minute has been used to better highlight some tendencies.

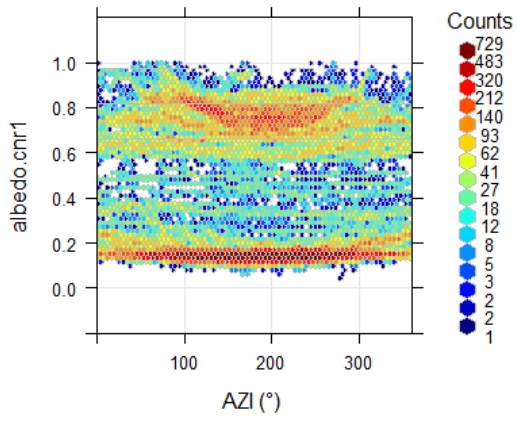

Figure 12: Albedo per minute values as a function of AZI during the year 2010

As shown in Figure 12, once again two distinct clusters are visible and, like previously discussed for the SZA, the upper one represents the spring conditions while the lower represents the summer season. What is interesting is that, using the values per minute, in the upper cluster a slight curve is clearly visible. In order to explain such behaviour, it is necessary to remember that such albedo values belong to the time of the year when the ground is covered in snow and ice and the prevailing wind blows from SE to NW. When the Sun rises during this time of the year, emerging slightly more towards the East each morning, its light reaches the ground and casts shadows in the north-western direction. As mentioned in the "Introduction", a typical phenomenon of snow-covered grounds is the presence of sastrugi, ice ridges oriented in the direction of the prevailing wind, born from the carving action of the wind on the icy surface. Since such structures are oriented in the SE-NW direction, their shadow is at its smallest in the morning, when sunlight is directed approximately like the wind and the surface in the shadows has the area of the smallest cross-section of the ridge. When the Sun reaches the South (AZI ~ 180), the shadow the sastrugi cast is bigger, and therefore the snow albedo gets reduced, since the areas in the shadow can reflect only the scattered light from the rest of the sky (only "white sky" albedo). As the

prevailing wind is not the only one blowing, this concept would need to be explored more to confirm this hypothesis, for example to prove that the smaller inclination of the westerly bulge in the graphic emerges exactly from such considerations, but this falls outside the intent of this thesis. This seems to be the right lead, though, since, looking at the lower cluster related to summer values, it is visible that the tundra is isotropic for reflection of SWD, being characterized by a non-regular distribution of lights and shadows.

Looking at the relation between SWD and AZI in Figure 13, the expected tendency is verified: the highest values of SWD happen when the Sun is shining from the southern direction, i.e. the central hours of the day when it reaches its minimum SZA. The outline of the graph represents once again the clear-sky condition summer days, while the data between the contour and the zero line belong to those days with Sun lower on the horizon (and less SWD incoming) or overcast conditions.

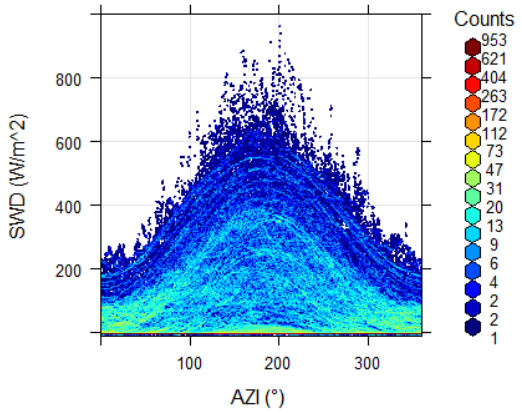

Figure 13: SWD values per minute collected in 2010 as a function of AZI

3.2.5 Annual behaviour

Finally, the annual behaviour of both shortwave and longwave radiation has been considered. More in depth analysis has been carried out on the longwave radiation and its relation with the temperature of the instruments, but laying outside the purpose of this thesis, it has been left out.

Daily averages have been computed and their evolution has been plotted over the course of the year. The behaviour of SW is plotted in Figure 14 and the portion of the year when the Sun doesn't rise on the horizon is clearly identifiable as the sections of the graphic where 0 W/m^2 are registered.

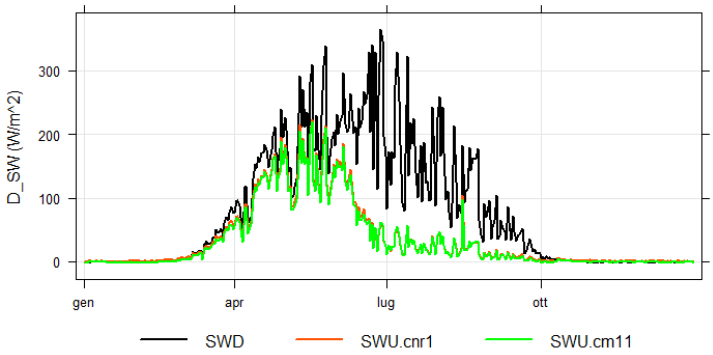

Figure 14: Daily averaged SWU, SWUcm11 and SWD values collected in 2010

Incoming SW follows the expected "bell shaped" outline, peaked in the summer months with irregular drops representing overcast conditions, mirrored by the reflected SWU. Another noticeable feature is the fact that SWU visibly lowers in the summer months: as the snow disappears from the ground, most of the radiation gets absorbed by the dark tundra instead of reflected and therefore SWU and albedo decrease.

Longwave radiation is emitted by the Earth itself all year round with enough intensity for the instruments to measure it even during polar night, so the curves in Figure 15 never reach zero. There is strong agreement between the values measured by CNR1 and CG4 and, as expected, LW lowers during the winter months and later grows in the summer, as the surface itself warms. Downwards

radiation follows the behaviour of LWU, measurements overlapping in certain areas suggesting periods of heavily cloud covered sky, when almost all the emitted radiation gets absorbed by the clouds and re-emitted towards the surface. The sudden drops in the LWD outline, on the other hand, represent the clear(er) sky conditions, when part of the radiation crosses the atmosphere and reaches outer space. To confirm the interpretation, comparing these last two graphics there is an exact matching between the deduced overcast or clear sky conditions, resulting in opposite behaviours in SWU and LWD.

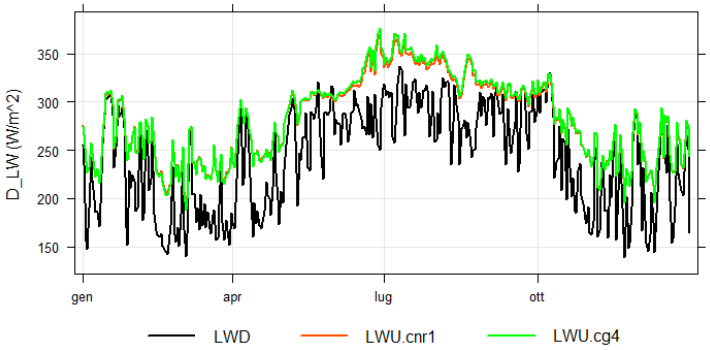

Figure 15: Daily averaged LWU, LWUcg4, LWD values collected in 2010

A shorter but similar analysis has been carried out for all the other years of available meaningful data, therefore the total period of analysis spans from 1/01/2010 to 3/8/2021, checking the sensibleness of the measurements taken and the proper functioning of the instruments on site .
Measurements are actually available from September 2009, but 2009 has not been considered in the following analysis since the melting season was not visible.

3.3 Regular and anomalous years

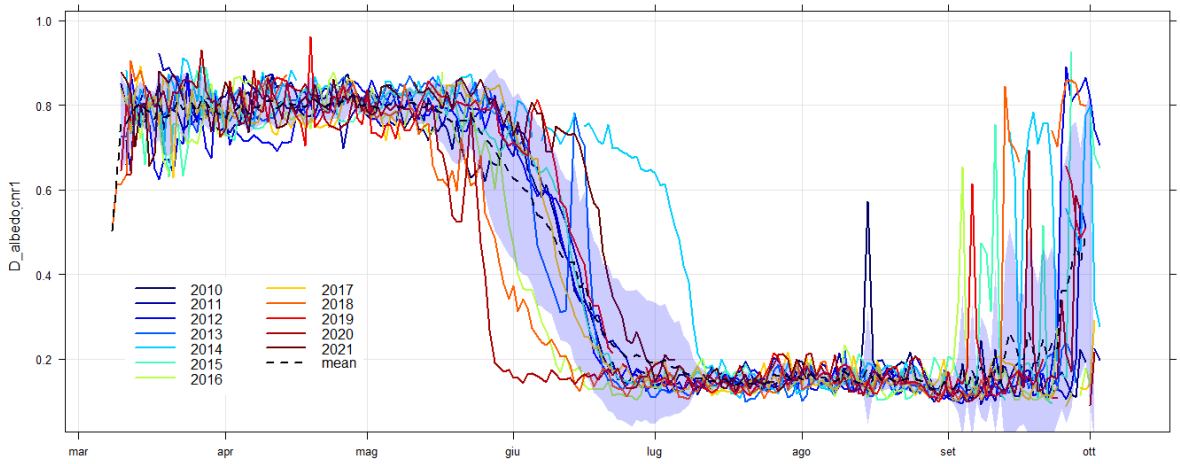

Figure 16: Daily albedo for the years 2010-2021 (solid lines), mean albedo over the years (dashed line) and shaded area representing 1 standard deviation (σ) around the mean

In order to identify a smoother behaviour of the albedo that nonetheless showed significant patterns, daily averages have been extracted. Then daily albedo has been plotted over the course of the year for all the years available, as shown in Figure 16. Average daily albedo over the course of the twelve year window (or eleven for the data from 4^{th} August onward) has been subsequently computed along with standard deviation of the sample and added to the plot.
The overall behaviour obviously shows the same pattern of the hourly averages and therefore the same interpretation applies. It is also visible that, though the melting season shifts and stretches through the years, there are some years that lay clearly outside the 1σ region, for example 2014 and 2020. The first represents a year when the snow cover of the ground lasted substantially longer compared to the others, while 2020 was an exceptional years for the opposite reason, as the snow vanished from the ground earlier and the albedo shows a steeper descent than any other year.
Such interpretation is supported also by pictures taken by the webcam pointing towards the bay from the Zeppelin Observatory, a research station rising near the top of Zeppelinfjellet, right above Ny Ålesund, operated by the Norwegian Polar Institute. There are two webcams, one fixed in the direction of the village (called "webcam") and one that rotates covering a wider angle (called "panorama") [16]. The new observatory dates back to 2000, but the pictures from the first 14 years have quite an irregular temporal coverage. Since 2015, though, a new fixed webcam has been used, and pictures were taken with higher resolution every 10 minutes with very few exceptions. This additional tool makes it possible to check the actual snow cover in the area surrounding the village, even though the CCT is not shown in the pictures, so it isn't possible to see directly if and how much snow there actually is under the tower. Having said that, over the course of the analyzed years the values of albedo computed with the CCT measurements implied a snow cover which was reasonably similar to the one that was visible from the Zeppelin pictures, so it has been assumed that the area surrounding the tower behaves similarly to the one framed by the webcam when it comes to presence of snow on the ground.
Another tool that allows us to have an idea of the presence of snow on the ground is the Ny Ålesund station of the Norsk Klimaservicesenter, active from 1974 and now managed by the Alfred Wegener Institute [15], which keeps track of daily mean snow depth. Such source of information has been used to indicatively locate the time period of interest, especially in the autumn where CCT observations were not available, and know in which days the relevant Zeppelin pictures had to be retrieved.

Focusing now on 2014, 2017 and 2020, i.e. years clearly above, within and below the average behaviour respectively, it's possible to verify, using these sources and the temperature and wind sensors at the top of the tower, that the melting took place at different times during said years.
The melting season is in fact, among other things, characterized temperature rapidly rising, without lowering again (occasional snowfalls aside) until the end of the season. If strong gusts of wind are present as well, they also play an important role in removing snow from the ground even more quickly than just by melting alone. Such behaviours are in fact seen during the days surrounding the period where albedo decreases in all the three years, as shown in the following Figure 17. Particularly relevant is the 2020 example, when higher winds blew during the melting that consequently happened much more quickly, as was already visible from Figure 16. Moreover, Zeppelin pictures taken before, during and by the end of such albedo descent show that snow on the ground did melt exactly as foreseen with the albedo analysis.
In Figure 17 the melting processes of the three selected years are visible: the pictures have been taken

for 2014 (aligned vertically) on 24/6, 5/7 and 16/7, for 2017 on 31/5, 9/6 and 23/6 and for 2020 on 12/5, 15/5 and 1/6. Daily albedo, temperature at 30m and hourly averaged wind speed between said dates are plotted as well.

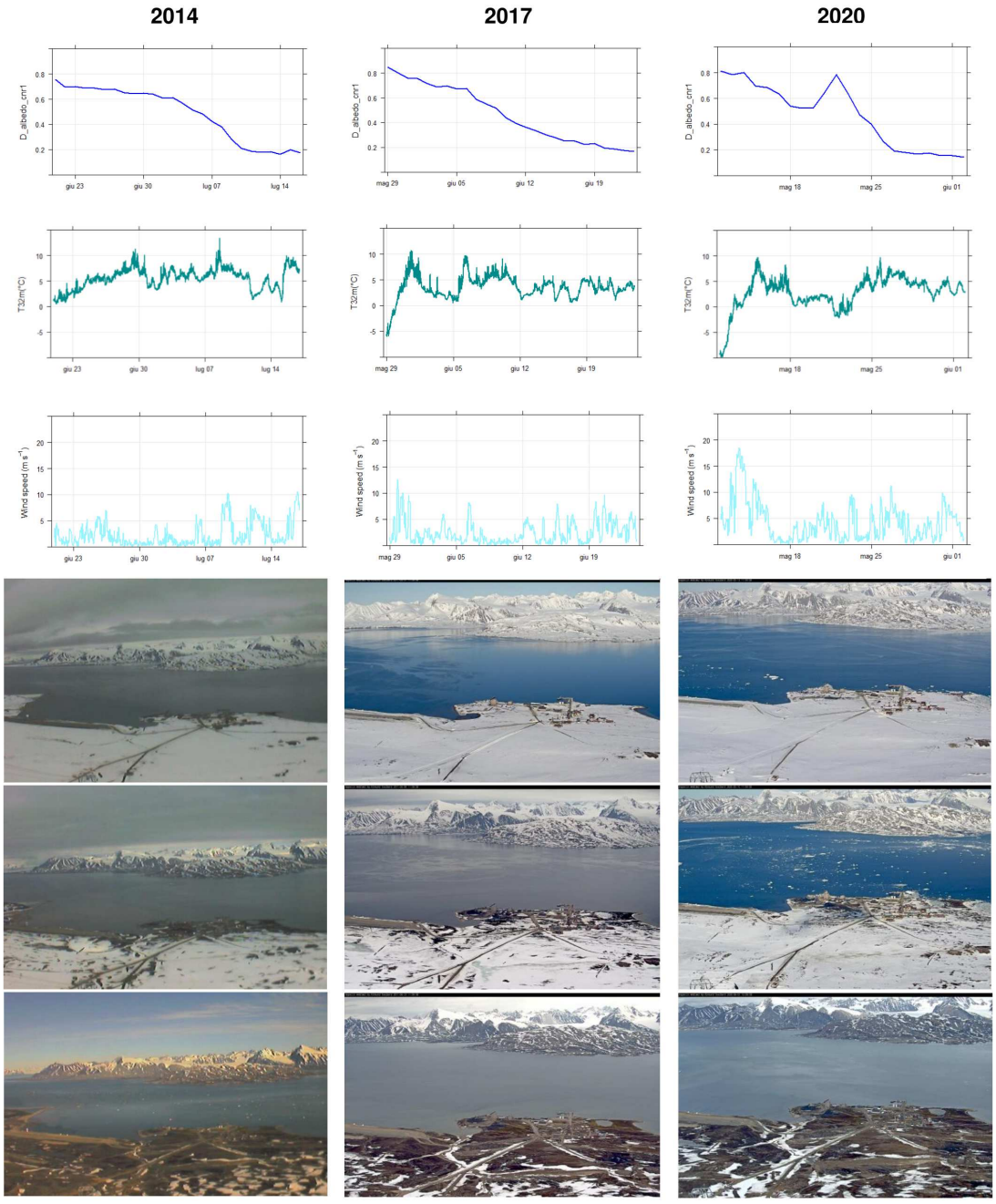

Figure 17: 2014, 2017, 2020 pictures of Ny Ålesund taken from the Zeppelin Observatory, daily albedo, temperature at 32m and wind speed in the same days

It is therefore clear that using albedo variations to infer snow cover of the ground is in fact a useful and precise way to determine features belonging to the melting window.

3.4 Melting season and Arctic summer

3.4.1 Melting season

In order to study the melting season, it has been decided to identify as precisely as possible the beginning and ending date. Once pinpointed such days of the year, it is possible to see if the length of the snow melting has varied during the years or if it has shifted on the calendar. Since, looking at the daily albedo behaviour over the course of the year, in some cases the albedo rises once again around September, implying the end of the summer season, it has been decided to try and determine for the years where it was possible the length of the Arctic summer as well.

It is therefore necessary to set some threshold to identify the periods of interest. Looking at Figure 16, during spring months the albedo experiences some oscillations, but rarely falls beneath 0.7 (except for the March window, that has already been discussed). The first time albedo actually goes below said value persistently is during the melting window. Moreover, comparing such insights with the pictures taken from Zeppelin during the following days pinpointed this way, it is possible to see that once albedo lowers beneath 0.7 the snow cover visibly becomes less homogeneous and greyer areas appear, later becoming spots of emerged grass and earth. Such process continues and, in the days corresponding to an albedo of 0.2, there is still some patches of snow, but they are few and far between and the tundra can be considered exposed. Looking at Figure 16 once again, it is in fact visible how during the summer albedo still fluctuates, but reaches at most the 0.2 boundary (except for occasional and not long lasting snowfalls). A 0.1 albedo seems to characterize completely exposed tundra and, in previous studies, a threshold of 0.1 has actually been used to identify the end of the melting window. In that case, though, the radiometer had been installed at a lower height, thus framing a smaller area. It is true that a 0.2 albedo implies the presence of some snow patches still on the ground, but even mid-summer albedo doesn't stay fixed on 0.1, and with an instrument installed in a higher location a far wider area is visible, with greater variability in the terrain morphology and distribution of shadows, so the 0.2 threshold has been considered more appropriate. The selected threshold values therefore are 0.7 for the beginning of the melting and 0.2 for the end.

It is necessary to estimate an error for the daily albedo, considering the instrumental uncertainty but also the fact that, during the course of the day, the Sun moves in the sky and the albedo computed at different hours of the same day can fluctuate for the reasons discussed in the "Instrumental analysis" section (dependency on SZA, AZI, geographical position and ice covered ground). Merely propagating the errors due to the instrumental accuracy means leaving out of the error all the other fluctuation causes, therefore underestimating the daily error. To avoid that, it has been decided to take as an estimate for the daily albedo error the standard deviation of the hourly diurnal values of albedo it was computed on. Once assigned an error to each daily average, a code has been written in R that compared every daily albedo with an interval centered on 0.7 and width determined by the error of the single daily albedo, i.e. $[0.7 - \sigma_{Dalbedo}; 0.7 + \sigma_{Dalbedo}]$. The same has been done for the 0.2 threshold. Where it was possible, the end of the Arctic summer was determined the as the day where the albedo rises again over 0.7 and does so for other five days, mirroring the analysis performed in the spring.

Carrying out the analysis, it has emerged that it was better to operate some corrections to the method in order to select the exact date.

First, since the daily averaged albedo still fluctuates consistently, around the edges of the melting period multiple days satisfied the selected conditions. It has therefore been decided to smooth the

data, averaging five days at a time. The code was then run on the smoothed data and on the hourly averages as well, to check that the smoothing hadn't removed some important oscillations that could shift the desired date.
Secondly, in order for a day to represent the beginning of the melting period, the agreed condition had to be verified both for that day and five days later, which allowed the program to exclude all those days during spring where albedo lowers around 0.7 only to rise again soon. The reversed condition has been applied to the 0.2 case, which meant that both the considered day and a day five days earlier had to verify the condition.
Finally, a visual check has been added using the pictures taken from the Zeppelin observatory, in order to be completely sure of the selected date.
The results of such analysis carried out in 2012 are represented in the Figure 18. In this case, smoothed data were useful at the beginning of the melting, but misleading by the end of it, since another snowfall took place covering the ground albeit briefly at the end of June.

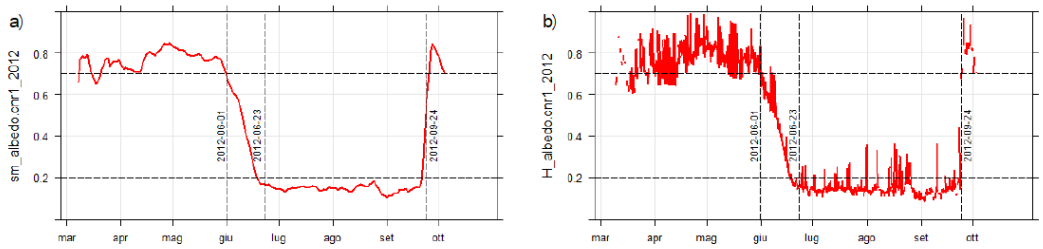

Figure 18: a) Daily smoothed and b) hourly albedo in 2012 with thresholds and timestamps

It is true that there are two sensors detecting SWU and therefore two values of albedo. From the information given in the "Instruments" section, the accuracy of CM11 is higher than the one of CNR1, therefore the initial idea was to use the values of albedo derived by CM11 measurements. Further considerations arose later in the analysis: even if CM11 values were more reliable, they were also systematically lower than the CNR1 ones, resulting in several occasions during the spring where albedo values were within 1σ from the 0.7 threshold for more than five days at a time, even though the ground was still perfectly mantled with snow. Another consequence was a shift in the moment where the albedo reached a certain threshold in the melting season. Due to the last snowfalls happening around the end of the melting, it often happened that CM11 values, usually preceding CNR1 ones, would once again reach the 0.2 threshold. Since snow would be once again visible for both sensors (confirmed by the Zeppelin camera), that had to be considered as the end of melting day, coinciding with the date simply determined with the CNR1. The total result was a widened melting season length, but only for the years that such combination took place, which eventually led to skewed results. Moreover, looking at the photos taken by the Zeppelin, the dates when CM11 albedo reached 0.2 still showed wide snow patches over the rest of the ground behind Ny Ålesund, that had considerably shrunk to a more reasonable size for a 0.2 albedo by the time CNR1 albedo reached it.
In order to avoid such problems, it has been chosen to use CNR1 albedo. Since the sensor is able to cover a wider area from the top of the tower, it is better suited especially to extract information regarding the end of melting window, where uneven snow patches might mislead the underlying sensor. Figure 19 is an example from 2020, where daily albedo was useful to determine the beginning but not the ending of the melting, and CM11 values would have lead to a wrong date since, as shown in the

hourly graphic, it snowed again on 28/05.

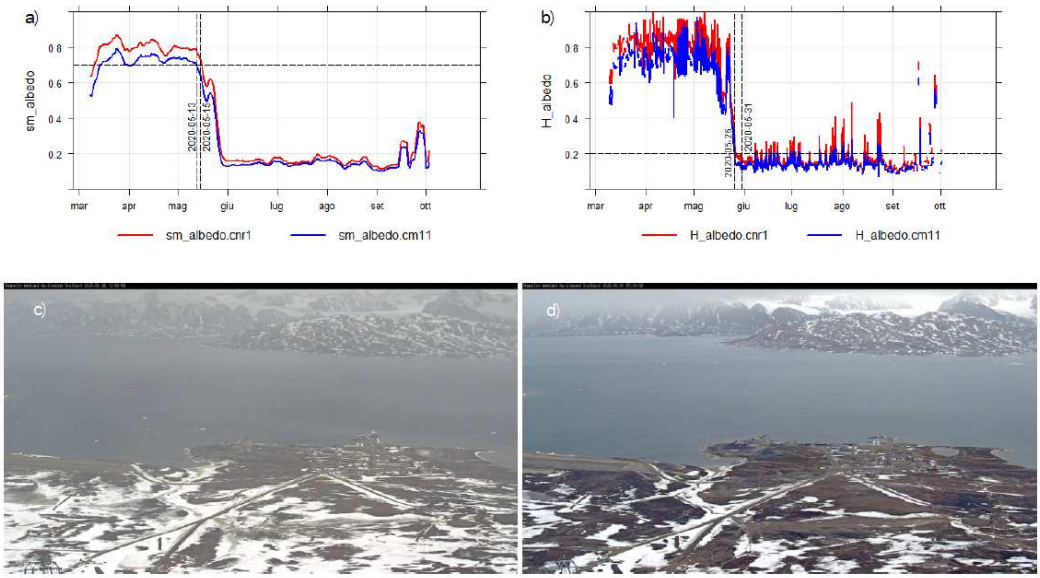

Figure 19: a)Daily smoothed and b)hourly albedo in 2020 with thresholds and timestamps, Ny Ålesund on c)26/05 and d)31/05/2020

3.4.2 Arctic summer

At first it looked like there were six years where autumn snowfalls were visible, even though albedo didn't reach 0.7 in all cases. Upon closer inspection, only in 2012 the snowfall visible from the CCT measurements covered the ground until spring. Thanks to the aid of the pictures taken at the Zeppelin and to the Norsk Klimaservicesenter website, it was possible to notice that for all the other years, even if albedo rose by the beginning of October (i.e. last days covered by the cleaned data), it was because of an early snowfall that would be later blown away by the winds, exposing the ground once more before the end of the year. In order to have a more precise parameter and a scenario easily recognizable in the Zeppelin pictures, Arctic summer has therefore been defined as the period that goes from the end of the melting season to the first time the snow falls in the autumn and does not melt anymore until the following spring.

Since albedo thresholds can't be used anymore beyond the beginning of October, the method hence developed takes advantage of the the Zeppelin observatory and the Norsk Klimaservicesenter station. Looking at the snow depth measurements collected from the station, it's possible to identify a range of dates where the definitive snowfall takes place. Downloading the Zeppelin pictures from those days it's possible to select the exact date, even if it happens when Ny Ålesund is already cloaked in polar night, since the whiteness of the ground is still clearly visible.

Figure 20 is an example of such analysis, when in 2019 the definitive snowfall happened on 16/10, as hinted by the graphic and confirmed by the pictures taken on 15/10 and 17/10 (16/10 was a series of white pictures since the webcam was in the middle of the snowstorm).

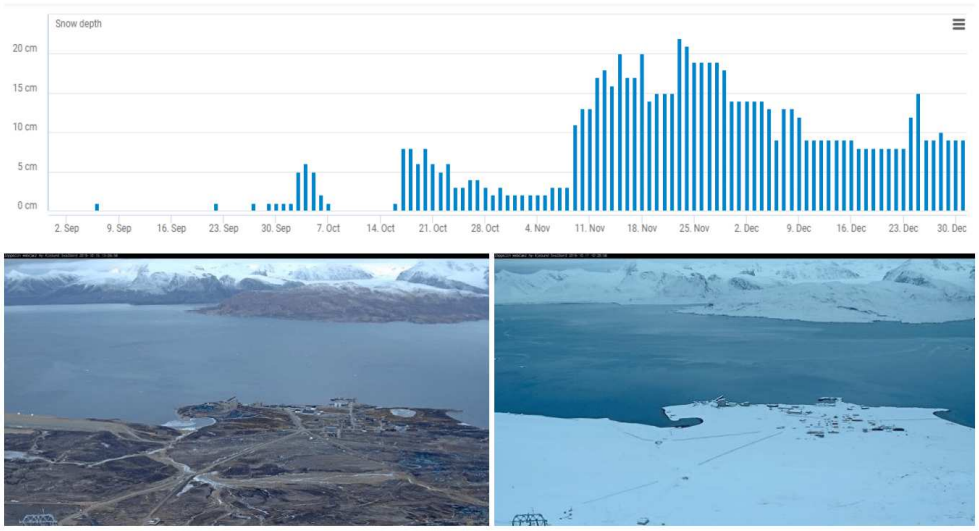

Figure 20: Snow depth (in cm) collected by the Norsk Klimaservicesenter [15], Ny Ålesund before (15/10) and after (17/10) the storm that took place on 16/10/2019

Using this combination of methods, a complete set of 12 years of dates was available for the melting season and of 11 years for the Arctic summer.
The selected dates have been translated into number of days from the beginning of the year in order to be better compared. The dates representing beginning and end of the melting season have been plotted as function of the respective year and, given the distribution of the plotted data, a linear fit has been applied. As visible from Figure 21, there is a decreasing trend, though in the last 2010s there have been some deviations from a more consistent behaviour in the first part of the decade, 2021 being second only to 2014 in the latest melting season. Looking at the beginning of the melting season, the regression line presents a slope of -0.5 ± 0.9 days per year, which means that the date when the snow starts to melt has moved back of 5 ± 9 days in a decade.
Similarly for the ending of the melting season, this date has moved back of 8 ± 9 days in a decade on the calendar.
The duration of the melting season has been studied as well: it ranges between 15 and 29 days, with an average value of 19 ± 1 days, decreasing quite constantly during the analyzed decade with little exceptions, such as 2018. Linear analysis has been applied as well and shows that the duration of the melting window has reduced of 3 ± 3 days in the last decade.

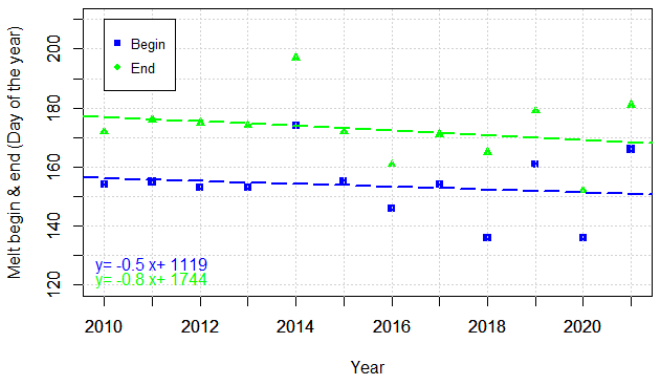

Figure 21: Estimated timing of melting process (start in blue, end in green) for 2010-2021

A similar analysis has been carried out on the number of summer days (Figure 22), computed as the number of days between the end of the melting season and the onset of persistent snow on the ground.

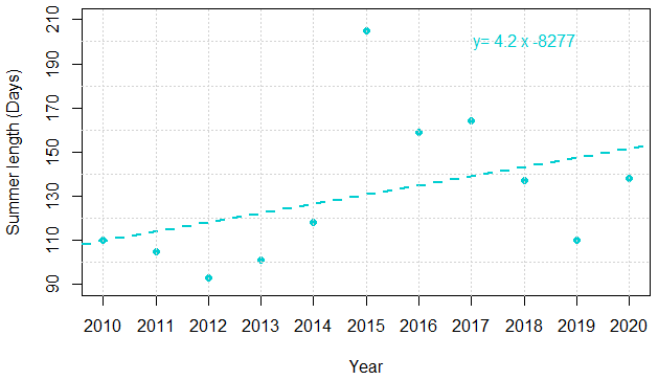

Figure 22: Estimated duration of Arctic summer in number of days for 2010-2020

2015 was the most anomalous year considered, as the first snowfall that managed not to be blown away by the wind took place in January 2016, even though the ground was surely frozen due to winter temperatures. As visible from the graphic, there is a strongly marked upward tendency in the data, confirmed by the regression line that shows a slope of 4 ± 3 days per year, resulting in a stretching of the summer season of 40 ± 30 days in a decade.

3.4.3 Net Surface Radiation Budget

Finally, it has been decided to analyze the Net Surface Radiation Budget (NSRB) and how it is related to the duration and timing of melting season and summer.

The years 2014, 2017 and 2020 have been studied further, as representative years of late, average and early melting. Figure 23 shows how the NSRB is affected by the late snowmelt in 2014, where long lasting snow contributed to reflecting a good portion of SWD, contrary to what happened in 2020 with an early snowmelt. Over the last six months all years behave rather similarly. In all cases the final snowfall took place around mid-October to November, therefore differences are due to weather conditions.

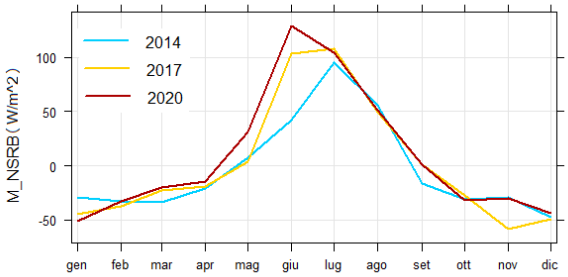

Figure 23: Monthly averaged NSRB in 2014, 2017 and 2020

In Table 2 there is a comparison of June NSRB, which obviously grows from 2014 to 2020. Surface absorbs this additional energy, which gets distributed in several ways that are difficult to quantify, but among them there is also atmospheric warming. Since temperature measurements are available both at 2 m and 32 m on the tower, it's possible to check how the bottom layer reacts to different NSRB. In 2014, when snow still covers the ground in June, temperature at 32 m is higher that at 2 m because it is warmed from radiation coming from the Sun above, while the snow reflects the majority of such radiation, acting as a cooling agent. In 2017 the melting process is still ongoing in June, so the difference in temperature is smaller, though still visible. The situation is inverted

	2014	**2017**	**2020**
Melt date (DOY)	174	154	136
June NSRB (W/m^2)	41.9±0.3	103.9±0.3	128.6±0.2
June T2m (°C)	1.95±0.05	3.56±0.05	3.87±0.05
June T32m (°C)	2.62±0.05	3.91±0.05	3.78±0.05

Table 2: Comparison of melt date, June NSRB, 2m and 32m temperature for 2014, 2017 and 2020

in 2020, where snow is already completely gone in June and the ground in this case absorbs solar radiation and warms, warming the lowest layer of air as well. Compared to an average melting year, this analysis suggests that the heating is not that significant anyway, since temperature only rises of about half a degree, therefore the additional energy must have been distributed in different ways.

The initial intention was to study how the total amount of radiation incoming in each year was connected with the differences in snow cover through the years, but since in some years during the winter there were several days of unavailable measurements, this meant that a whole section of (surely negative) NSRB wasn't included in the computation and the overall effect was an unreliable depiction of yearly NSRB where dependencies from the melt date were erased. In order to avoid this problem, it has been decided to split the computation in the two seasons of interest: in the following discussion, "summer" refers to the days from mid-May to the end of August, while "autumn" refers to the period between the beginning of September and the end of November, where in nearly all cases (2015 aside) the last snowfall takes place. The NSRB in these seasons for the different years has been plotted in function of the melt date (in days of the year).

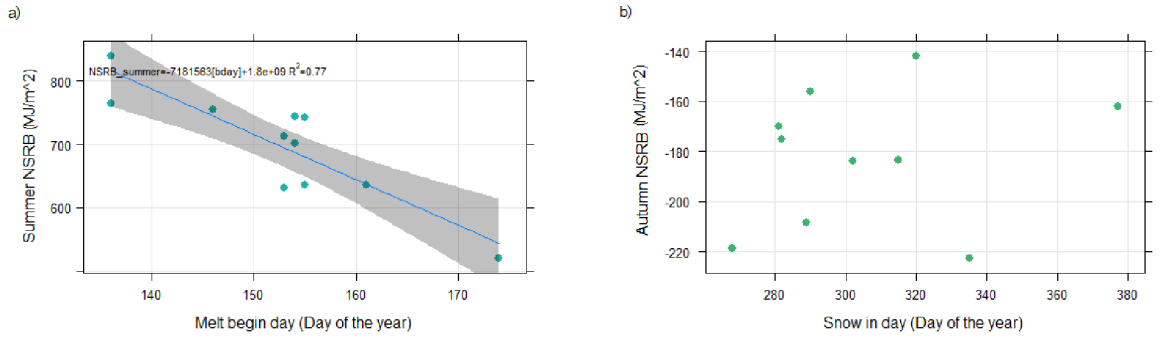

Figure 24: a) Scatterplot of Summer NSRB and the day the melt starts for the years 2010-2020; b) Scatterplot of Autumn NSRB and the day the final snowfall happens for the years 2010-2020

As clearly visible in the Figure 24a, there is a connection between the retreating of the melting season and the net radiation, leading to 7 ± 1 MJ/m^2 in total on the surface for each day the melt advances, which is $\sim 1\%$ of summer total energy budget. This means that, using previous results, for a retreat of 5 ± 9 days Ny Ålesund gains 35 ± 63 MJ/m^2 of energy or 1 ± 2 W/m^2 on an annual basis. Looking at the autumn NSRB in Figure 24b, the graphic shows how there is not such a strong connection between the date of the last snowfall and the net radiation collected during those months and, as a consequence, on the yearly budget. Consequently, the most significant factor in determining the yearly net radiation total is the date of the snowmelt. The months going from May to August are in fact the ones where the most of the Sun's radiation hits Ny Ålesund, so a variation on how much of such radiation gets reflected away from the surface instead of being absorbed, which is directly linked to how early the snow melts during those months, has a huge impact on the yearly budget. From September to November the Sun slowly sets, disappearing completely around the end of October, so the most relevant component in the net radiation is the longwave, which is influenced by the presence of snow on the ground, but not as strongly as the shortwave is.

Lastly, the radiation profile of the whole 11-years dataset has been studied with monthly averages over the observation period, both separating the SW and LW components and considering the whole net budget. While SW is always positive, as the received radiation is considered positive and is always more than the reflected, LW is negative instead, since outgoing radiation is considered negative and the atmosphere returns back only a fraction of it. The greatest shortwave budget variability is seen during the spring an summer months: different cloud cover conditions through the years influence the amount of SWD reaching the surface, while modifications in surface properties during the snow melt season affect SWU according to the time they took place on different years. LWD variability comes from atmospheric temperature and sky conditions, while LWU depends on snow cover and surface temperature. Significant variations are seen during polar night as well, due to the large variability in in atmospheric temperature and humidity and on the radiative effect of clouds [9]. Such considerations agree with and confirm the results of a precedent similar analysis run by AWI researchers from 1992 to 2012 [8].

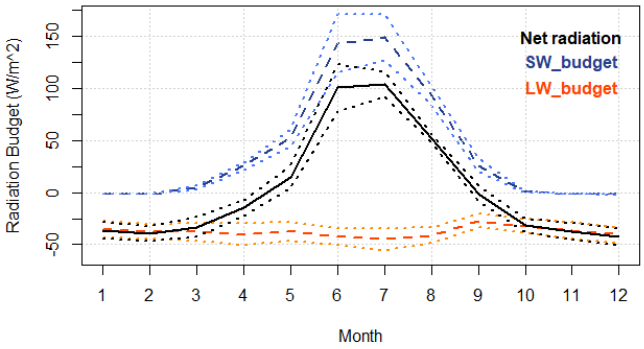

Figure 25: Net surface monthly radiation budget, SW budget and LW budget averaged from 2010 to 2020 (thicker lines) and $\pm 1\sigma$ (thinner lines)

4 Conclusions

Aim of this thesis was to study radiative fluxes in Ny Ålesund thanks to measurements collected by the Climate Change Tower, investigating the melting season in the Arctic using broadband albedo. The end of Arctic summer has been studied as well, since it appeared to be included in albedo measurements, but more in depth analysis led to a different method of investigation. The dataset analyzed ranged from January 2010 to the beginning of August 2021 and included measurements of upwards and downwards shortwave and longwave radiation collected every minute, along with meteorological parameters such as temperature, wind speed and direction.

From this study it emerges that the beginning of melting season has retreated of 5 ± 9 days in a decade and its duration has decreased as well of 3 ± 3 days in a decade, with the time of snow disappearance shifting to an earlier date by 8 ± 9 days. The end of summer, identified in this study as the first snowfall that persists on the ground until the following spring, has instead advanced towards the end of the year of 40 ± 30 days in a decade. The shifting in the melting season has led to a 1 ± 2 W/m^2 rise in the net surface energy budget on an annual basis. While this may seem a little amount, previous studies show that only a 1.0 W/m^2 increase in net surface radiation can increase global air temperature by $\sim 0.6°C$ [10]. The lengthening of Arctic summer, instead, doesn't imply a significant variation on the net yearly budget.

Similar studies carried out in recent years, in the same location and with the same thresholds have also found evidence of an anticipation of the first snow free day. The AWI group has provided quality-controlled surface radiation measurements to the Baseline Surface Radiation Network (BSRN) since 1992. For the 2015 study they selected a dataset ranging from 1992 to 2012, collected at the AWI station south of Ny Ålesund with a radiometer installed a lower height, thus capable of seeing a smaller area. The research group has determined that the time of snow melt had retreated of 4.8 ± 8.3 days per decade [8]. More recently, a study led by ISP has analysed an even longer time window, ranging from 1981 to 2019 merging three different datasets collected in Ny Ålesund: 1981 to 1997 collected from the Norwegian Polar Institute, 1993 to 2019 from AWI and 2009 to 2019 from the CCT. The results state that the first day of snow gone has retreated of 3 ± 1 days per decade [11]. The oldest of such datasets comes from a 2002 study led by Norwegian researchers who, using a lower threshold for snow gone albedo (0.1) and collecting data at low height, had found no significant trend or indication of climate change [12].

Even though the setup conditions in the Norwegian and AWI datasets were different, it is quite clear from the comparison between these estimates that the results of this thesis could grow in precision and significance if more years were considered in the analysis. A longer time window would in fact allow for atypical years to have a lesser influence on the final result, with the additional advantage of obtaining relevant results on a climatic time scale. A way to improve the results obtained from this dataset for further studies without including more years would be to better analyse sky conditions, conducting separate studies in the clear sky days and in overcast days. Given the blue, black and white-sky albedo definition in the "Instrumental analysis" section, it is clear that cloud cover influences such parameter and a more refined analysis could lead to more precise results. Moreover, in order to further investigate the consequences of the additional energy on the uppermost snow layer during the melting season, this study could be broadened using temperature measurements taken

from within the snow layer. These measurements are collected by CCT, but belong to separate set of instruments and would need pre-analysis on their calibrations. Finally, given the decisive role played in this study by the webcam coverage of the measurement site, further study should try to extract even more information from such pictures, for example to support an analysis on the sky conditions or even to better estimate the percentage of surface still covered in snow during the melting season on a wider area compared to the one seen by the instrument.

That being said, radiometric measurements are of crucial importance for monitoring and understanding the changing climate, specifically the snowpack conditions in this case. Surface albedo computed from such measurements is a simple yet precise way to keep track of climate variations and can be implemented also in remote stations located in harsh environments at high latitude where other techniques might be hindered. Given a deeper analysis and a more extended time window, it promises to lead to more meaningful results.

Bibliography

[1] Wallace J. and Hobbs P. *Atmospheric Science: An Introductory Survey*. II. Academic Press, 2006.

[2] Masson-Delmotte V. et al. *IPCC, 2021: Climate Change 2021: The Physical Science Basis. Contribution of Working Group I to the Sixth Assessment Report of the Intergovernmental Panel on Climate Change*. Tech. rep. 2021.

[3] Serreze M. C. and Barry R. G. "Processes and impacts of Arctic amplification: A research synthesis". In: *Global and Planetary Change* 77.1 (2011), pp. 85–96.

[4] Pithan F. and Mauritsen T. "Arctic amplification dominated by temperature feedbacks in contemporary climate models". In: *Nature Geosciences* 7.3 (2014), pp. 181–184.

[5] Goosse H., Kay J.E., and Armour K.C. et al. "Quantifying climate feedbacks in polar regions". In: *Nature Communications* 1919 (Sept. 2018).

[6] Stuecker M. et al. "Polar amplification dominated by local forcing and feedbacks". In: *Nature Climate Change* 8 (Dec. 2018).

[7] Spencer J.W. "Comments on The Astronomical Almanac's Algorithm for Approximate Solar Position (1950-2050)". In: *Solar Energy* 42 (4 1989), p. 353.

[8] Maturilli M., Herber A., and König-Langlo G. "Surface radiation climatology for Ny-Ålesund, Svalbard (78.9° N), basic observations for trend detection". In: *Theoretical and Applied Climatology* 120 (1 2015), pp. 331–339.

[9] Maturilli M., Herber A., and König-Langlo G. "Climatology and time series of surface meteorology in Ny-Ålesund, Svalbard". In: *Earth System Science Data* 5 (1 2013), pp. 155–163.

[10] Stone R.S. et al. "Earlier spring snowmelt in northern Alaska as an indicator of climate change". In: *Journal of geophysical research* 107 (D10 2002), ACL 10-1-ACL 10–13.

[11] Becherini F. et al. "Surface albedo and spring snow melt variation at Ny Ålesund, Svalbard". In: *Bulletin of Atmospheric Science and Technology* (2021, Submitted).

[12] Winther J.G. et al. "Surface albedo in Ny-Ålesund, Svalbard: variability and trends during 1981–1997". In: *Global and Planetary Change* 32 (2-3 2002), pp. 127–139.

[13] Institute of Polar Sciences. *Climate Change Tower*. URL: `https://www.isp.cnr.it/index.php/en/infrastructures/observation-facilities/cctower`.

[14] Norsk Polarinstitutt. *Kongsfjorde Map*. URL: `https://www.npolar.no/en/maps/`.

[15] Norsk Klimaservicesenter. *Ny Ålesund station*. URL: `https://seklima.met.no/stations/`.

[16] AWI - Zeppelin Observatory. *Pictures from the Zeppelin Observatory*. URL: `https://data.npolar.no/_file/zeppelin/camera/`.

[17] CNR. *Italian Arctic Data Center*. URL: `http://iadc.cnr.it/cnr/`.

[18] Kipp and Zonen. *Kipp and Zonen CMP11 Pyranometer*. URL: `https://www.kippzonen.com/Product/13/CMP11-Pyranometer`.

[19] Kipp and Zonen. *Kipp and Zonen CG4 Pyrgeometer*. URL: https://www.kippzonen.com/Product/17/CGR4-Pyrgeometer.

[20] Kipp and Zonen. *Kipp and Zonen CNR1 Net Radiometer*. URL: https://www.campbellsci.com/cnr1.

Acronyms

AWI	Alfred Wegener Institute for Polar and Marine Research
AZI	azimuth
BSRN	Baseline Surface Radiation Network
CCT	Climate Change Tower
D - ↓	down
IPCC	Intergovernmental Panel on Climate Change
ISP	Istituto di Scienze Polari
LW	longwave
NSRB	Net Surface Radiation Budget
SW	shortwave
SZA	solar zenith angle
U - ↑	up